Supplementary information

Probing the critical nucleus size for ice formation with graphene oxide nanosheets

Guoying Bai, Dong Gao, Zhang Liu, Xin Zhou & Jianjun Wang

Supplementary Information for

Probing the critical nucleus size of ice formation with graphene oxide nanosheets

Guoying Bai[1,2], Dong Gao[3], Zhang Liu[1], Xin Zhou[4,5,6]★, and Jianjun Wang[1,6,7]★

[1] Key Laboratory for Green Printing, Beijing National Laboratory for Molecular Science, Institute of Chemistry, Chinese Academy of Sciences, Beijing 100190, P. R. China.

[2] Research Institute for Energy Equipment Materials, School of Materials Science and Engineering, Hebei University of Technology, Tianjin 300401, P. R. China.

[3] Key Laboratory of Hebei Province for Molecular Biophysics Institute of Biophysics, Hebei University of Technology, Tianjin 300401, P. R. China.

[4] School of Physical Sciences and CAS Center for Excellence in Topological Quantum Computation, University of Chinese Academy of Sciences, Beijing 100049, P. R. China

[5] Wenzhou Institute, University of Chinese Academy of Sciences, Wenzhou, P.R. China

[6] Songshan Lake Materials Laboratory, Dongguan, Guangdong 523808, P. R. China

[7] School of Future Technology, University of Chinese Academy of Sciences, Beijing 100049, P. R. China.

Corresponding authors: E-mail: xzhou@ucas.ac.cn (X. Z.); wangj220@iccas.ac.cn (J. W.)

Table of Contents:

PS1: Characterizations of GOs.

Supplementary Fig. 1 | Hydrodynamic diameter distributions of GOs of controlled sizes. Typical hydrodynamic diameter distributions of various size-fractioned GO samples measured by dynamic light scattering spectrometer. The results confirm GOs of controlled sizes were obtained.
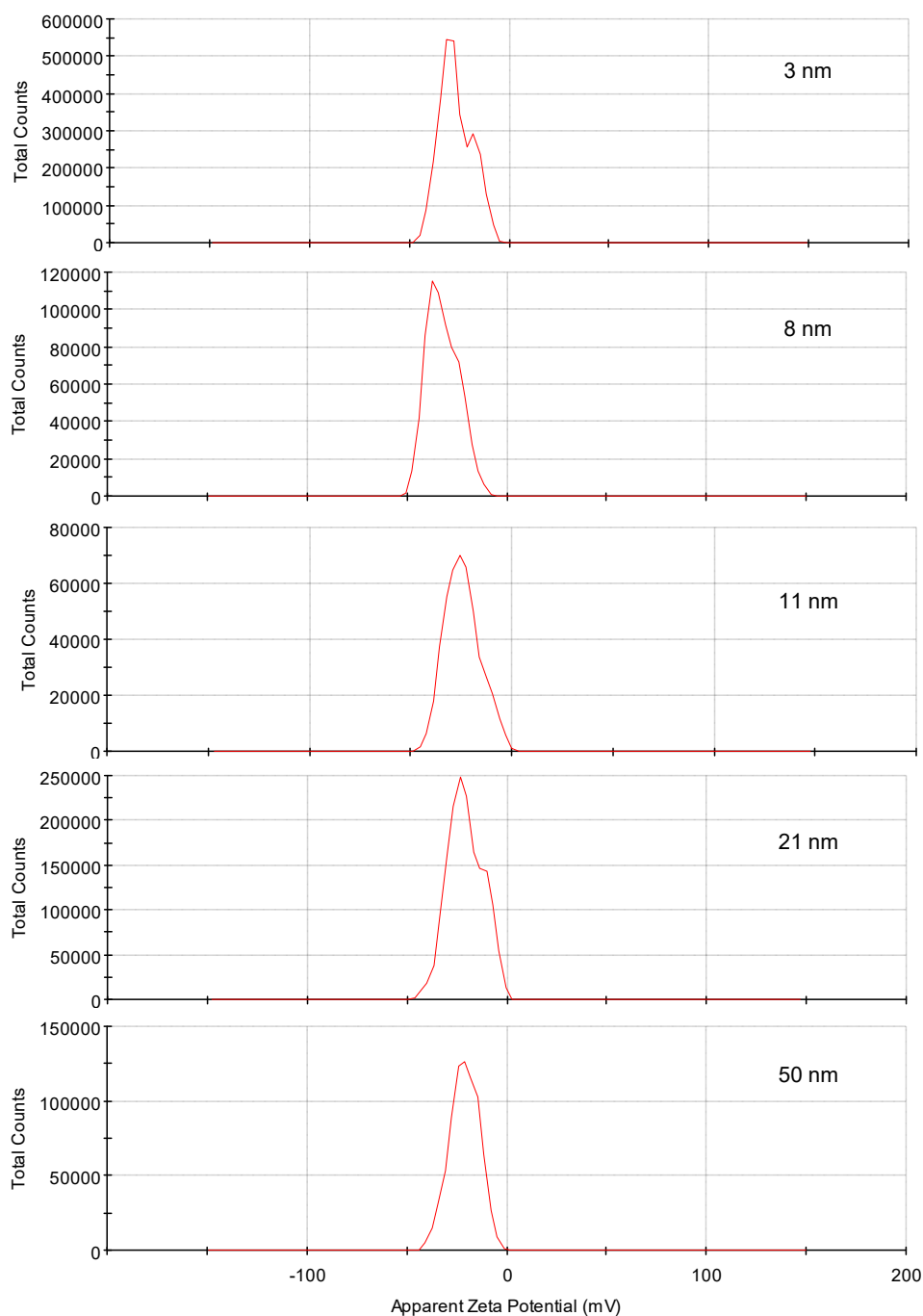
Supplementary Fig. 2 | Zeta potential distributions of GOs of controlled sizes. Typical zeta potential distributions of GOs with different average lateral dimensions measured by Malvern Zetasizer. The negative zeta potentials of GO samples contribute to their good dispersibilities in water.
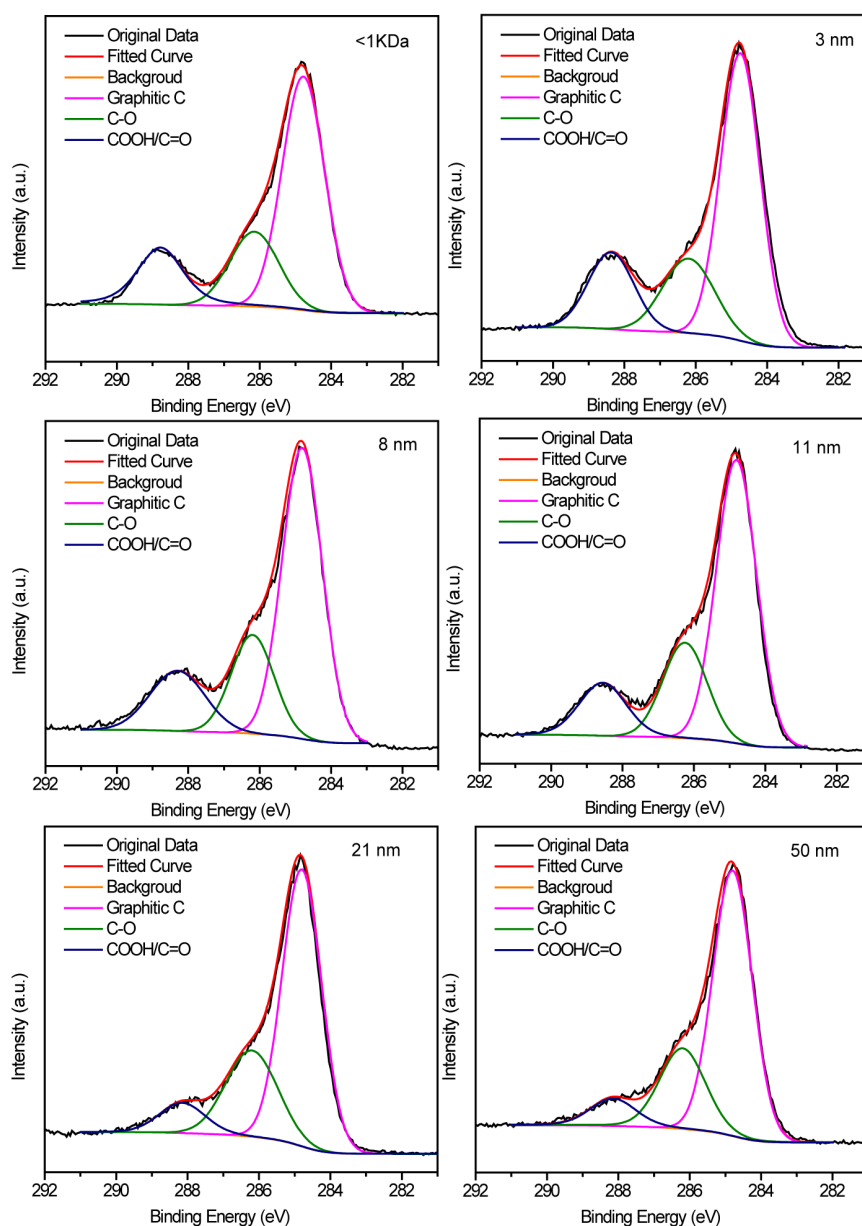
Supplementary Fig. 3 | C1*s* core-level X-ray photoelectron spectroscopy (XPS) spectra of GOs of controlled sizes. C1*s* spectra of six GO fractions can be deconvoluted into three Gaussian peaks attributed to graphitic C (284.8 eV), C-O (286.2 eV) and COOH/C=O (288.3 eV), respectively.[1]

The element content analysis results (listed in Extended Data Table 1) indicate that the C/O atomic ratio increases slightly with the increase of GO size, which is consistent with previous reports.[2,3] The slight decrease of the oxidation extent with the increase of GO size is mainly ascribed to the reduction in the content of COOH/C=O groups which are mostly located at the edges of GOs, based on the C1*s* core-level XPS spectra.
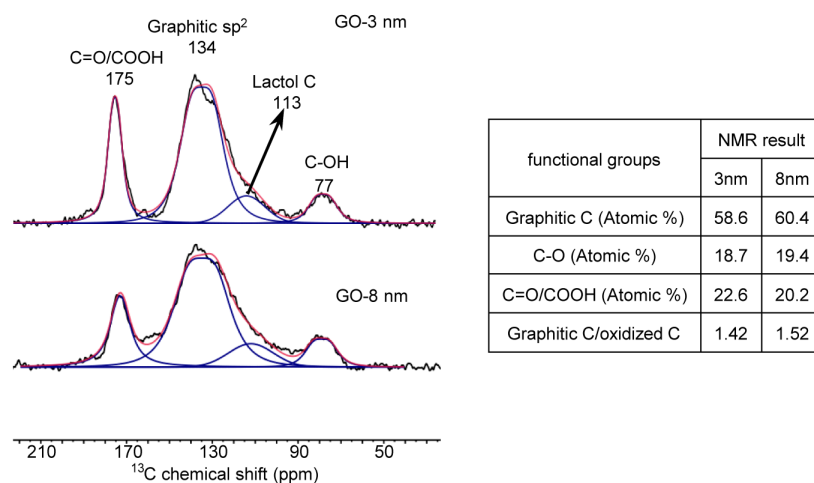
Supplementary Fig. 4 | Solid-state ^{13}C high-power proton decoupling (HPDEC) nuclear magnetic resonance (NMR) spectra of GOs with the average lateral size of 3 and 8 nm. The right table shows the ratios of various carbon-containing functional groups. 15360 scans were accumulated in order to obtain a good signal to noise ratio.

The spectra were fitted by deconvolution method to separate the crowded peaks, which are attributed to COOH/C=O (*ca.* 175 ppm), graphitic C (*ca.* 134 ppm), lactol C (*ca.* 113 ppm), and C-OH (*ca.* 77 ppm), respectively.[4,5] And the ratios of various carbon-containing functional groups were obtained by the area ratios of the corresponding peaks. The percentage contents of various functional groups were compared between the results obtained by NMR (the right table in Supplementary Fig. 4) and XPS (Extended Data Table 1). It is obvious that the ratios between graphitic C and oxidized C obtained by two methods are almost the same.
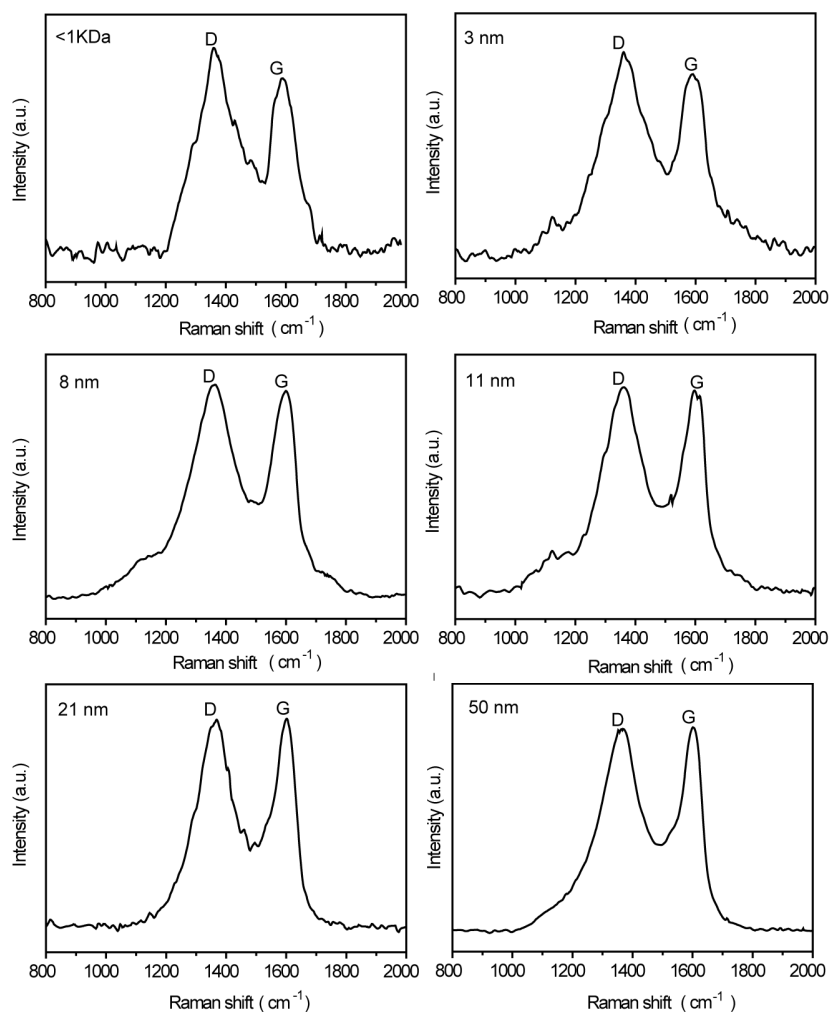
Supplementary Fig. 5 | Raman spectra of GOs of controlled sizes. Raman spectra of GO samples with different average lateral sizes feature typical D and G bands located at 1359 and 1592 cm^{-1}, respectively.[6] The ratios of I_D/I_G show a slight decrease with the increase of the GO size, indicating that larger GO has a little lower defect density[7,8].
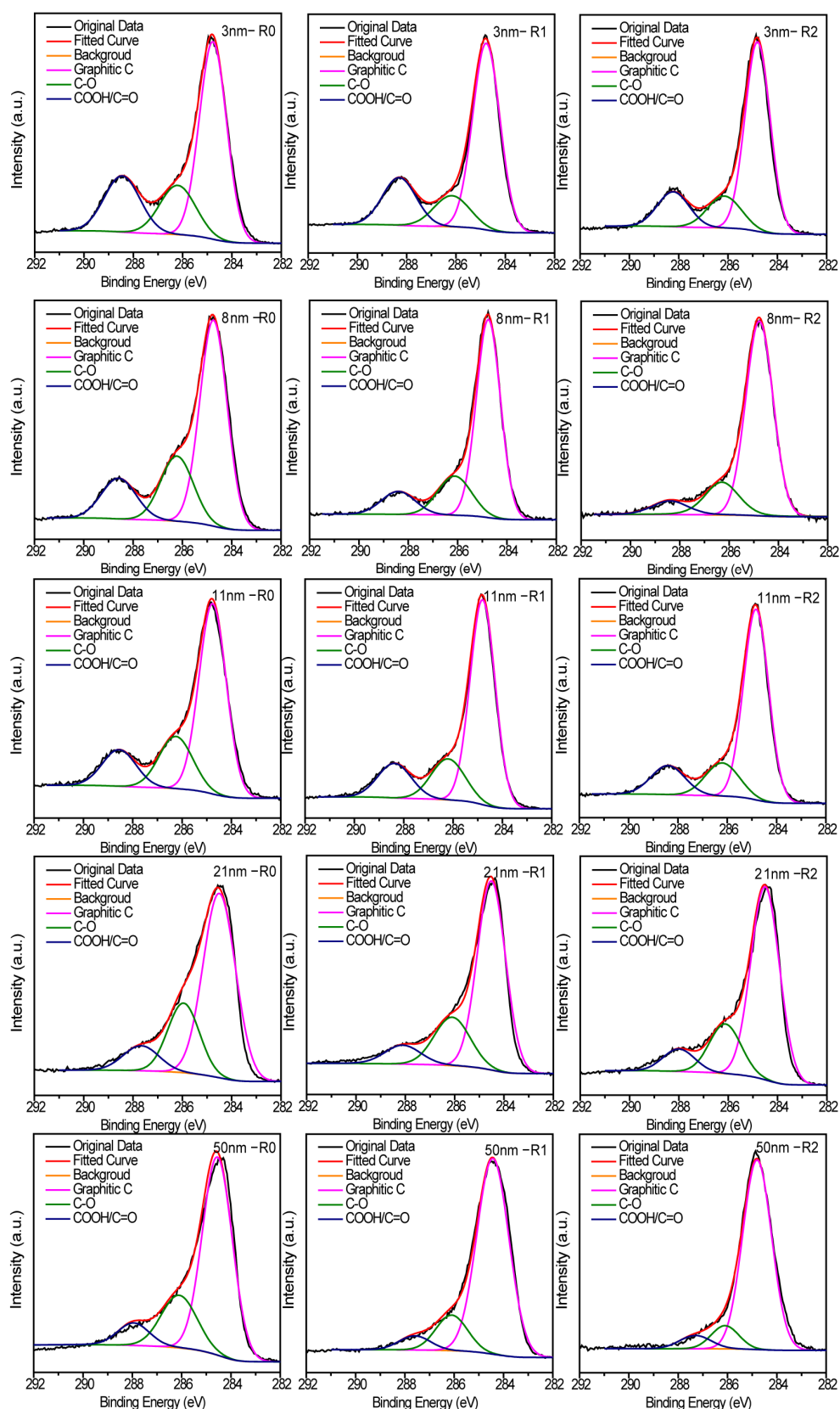
Supplementary Fig. 6 | C1*s* core-level XPS spectra of GOs with controlled sizes and decreasing oxidation degrees. R0, R1 and R2 represent the GOs without alkali treatment and with the alkali treatments at pH=10 and 12, respectively.
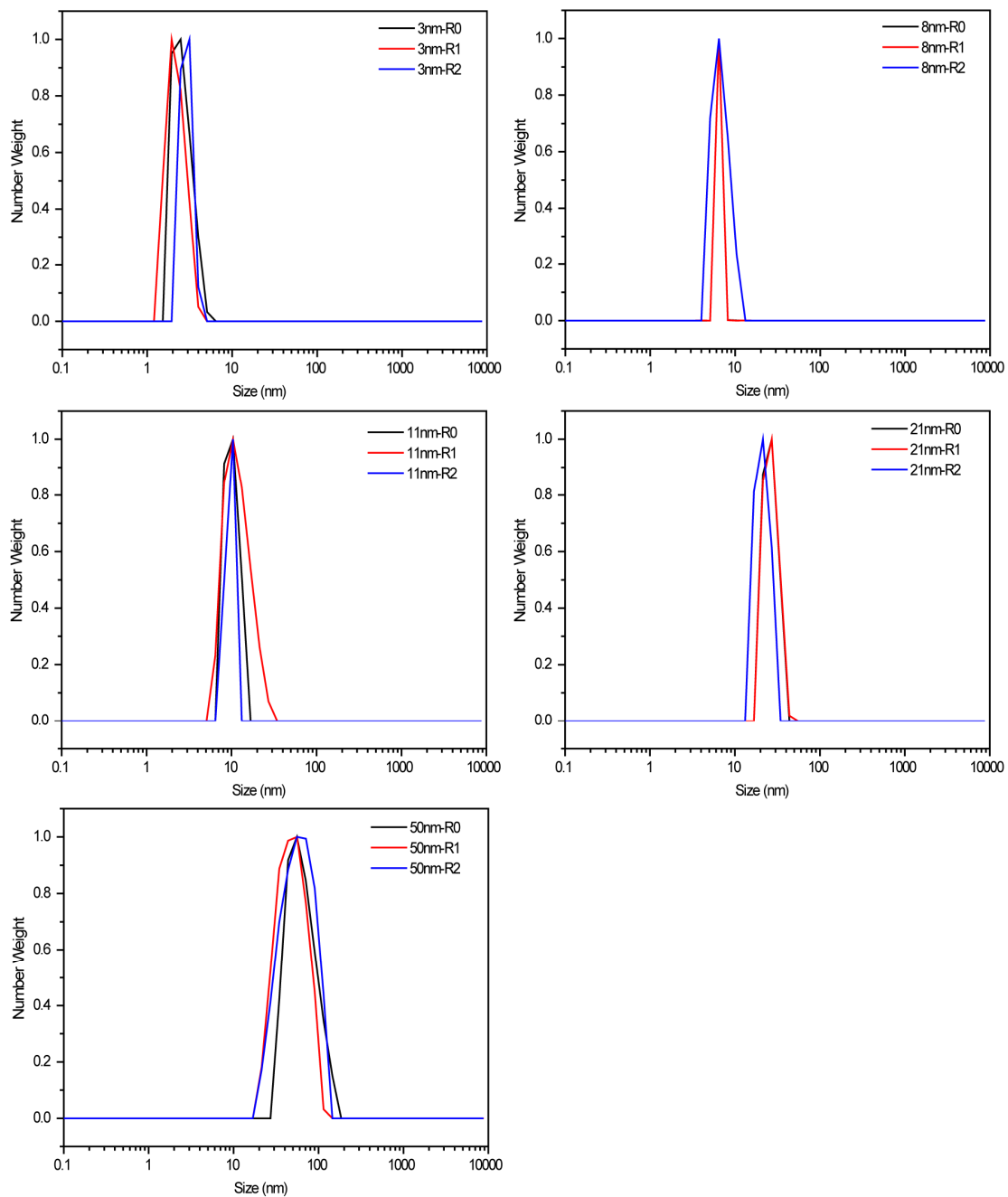
Supplementary Fig. 7 | Typical hydrodynamic diameter distributions of GOs with controlled sizes and decreasing oxidation degrees measured by dynamic light scattering spectrometer. R0, R1 and R2 represent the GOs without alkali treatment and with the alkali treatments at pH=10 and 12, respectively.
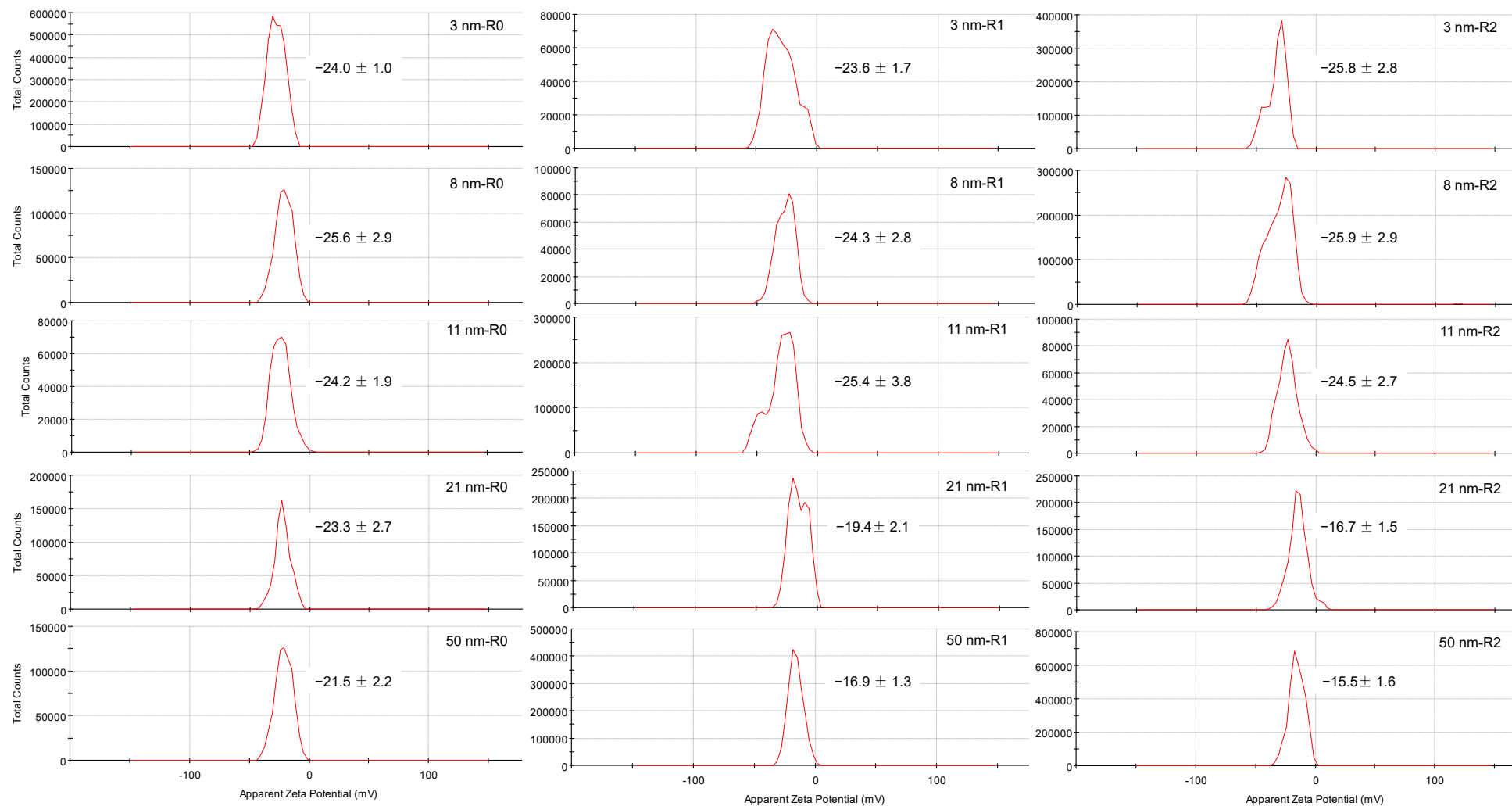
Supplementary Fig. 8 | Typical zeta potential distributions of GOs with controlled sizes and decreasing oxidation degrees measured by Malvern Zetasizer. R0, R1 and R2 represent the GOs without alkali treatment and with the alkali treatments at pH=10 and 12, respectively. Data are means ± s.d. The measurement number for each sample is 3.
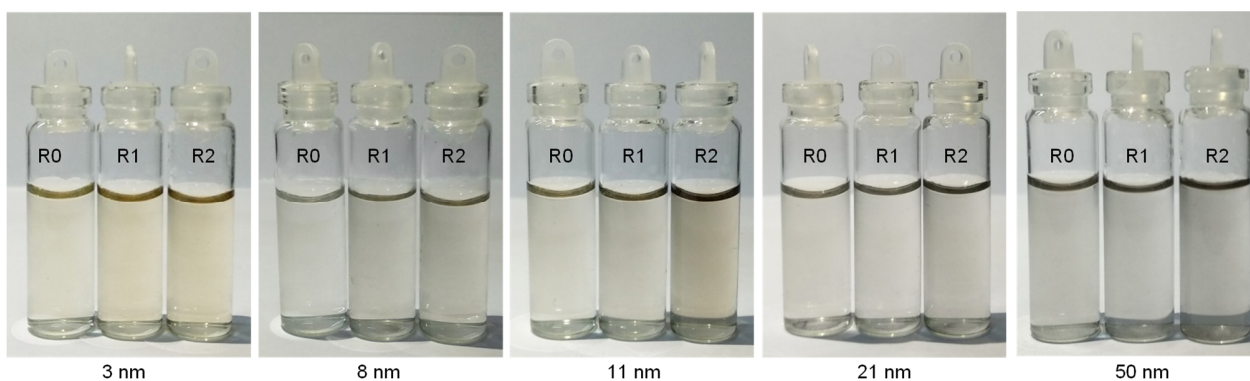
Supplementary Fig. 9 | Photographs of aqueous dispersions containing GOs with controlled sizes and decreasing oxidation degrees (0.04 mg ml⁻¹). R0, R1 and R2 represent GO samples without alkali treatment and with alkali treatment at pH=10 and 12, respectively. All the GO aqueous dispersions are clear and transparent, indicating the well dispersibility of various GOs in water.

PS2: Analysis of Variance on T_{IN} data of water droplets containing GOs of controlled sizes for statistical significance

One-way ANOVA was performed on T_{IN} data of water droplets containing GOs with a series of sizes in Fig. 2b of the main text for statistical significance. The results show that the T_{IN} difference is caused by the size, and T_{INS} for 3 and 8 nm have no statistical difference but the others have statistical difference. We take the T_{IN} for different-sized GOs (concentrations: 13 μmol L^{-1}, cooling rate: 5 °C min^{-1}) as an example.

Summary

group	number	sum	mean	variance
3nm	167	−4540.9	−27.191	5.656124
8nm	150	−4102.8	−27.352	5.109895
11nm	163	−2899.1	−17.7859	6.657763
21nm	212	−3587.2	−16.9208	2.351416
50nm	169	−2651.9	−15.6917	3.675288

Test for homogeneity of variance

Levene statistic	df1	df2	Statistical significance
16.346	4	856	0.000

ANOVA

Source of variance	SS	df	MS	F	Statistical significance
SS$_{treatments}$	22322.84	4	5580.71	1227.272	0.000
SS$_{error}$	3892.446	856	4.547249		
SS$_{total}$	26215.29	860			

As the distributions of T_{IN} for different-sized GOs do not meet the requirement of homogeneity of variance, we also performed Welch test and Brown-Forsythe test which do not require the homogeneity of variance.

	Statistics	df1	df2	Statistical significance
Welch	1217.637	4	404.308	0.000
Brown-Forsythe	1180.952	4	727.166	0.000

All the results show that the T_{IN} difference is caused by size.

To further investigate how size influences T_{IN}, we performed multiple comparisons. As shown in the following table, T_{IN}s for 3 and 8 nm have no statistical difference but the others have statistical difference.

Multiple comparisons

	(I) Size (nm)	(J) Size (nm)	Difference of the mean (I-J)	Standard Error	Statistical significance	95% confidence interval	
						lower limit	upper limit
Tamhane	3	8	0.1609820	0.2606434	1.000	−0.573890	0.895854
		11	−9.4051284*	0.2733389	0.000	−10.175620	−8.634636
		21	−10.2702632*	0.2120391	0.000	−10.868793	−9.671734
		50	−11.4993020*	0.2358310	0.000	−12.164157	−10.834447
	8	3	−0.1609820	0.2606434	1.000	−0.895854	0.573890
		11	−9.5661104*	0.2736990	0.000	−10.337858	−8.794363
		21	−10.4312453*	0.2125031	0.000	−11.031616	−9.830874
		50	−11.6602840*	0.2362482	0.000	−12.326700	−10.993868
	11	3	9.4051284*	0.2733389	0.000	8.634636	10.175620
		8	9.5661104*	0.2736990	0.000	8.794363	10.337858
		21	−0.8651349*	0.2278964	0.002	−1.508893	−0.221376
		50	−2.0941736*	0.2501848	0.000	−2.799813	−1.388534
	21	3	10.2702632*	0.2120391	0.000	9.671734	10.868793
		8	10.4312453*	0.2125031	0.000	9.830874	11.031616
		11	0.8651349*	0.2278964	0.002	0.221376	1.508893
		50	−1.2290387*	0.1812149	0.000	−1.739928	−0.718150
	50	3	11.4993020*	0.2358310	0.000	10.834447	12.164157
		8	11.6602840*	0.2362482	0.000	10.993868	12.326700
		11	2.0941736*	0.2501848	0.000	1.388534	2.799813
		50	1.2290387*	0.1812149	0.000	0.718150	1.739928

*Significance level of difference of the mean is 0.05.

PS3: Ice nucleation probability distributions of water droplet containing GOs of controlled sizes and decreasing oxidation degrees.
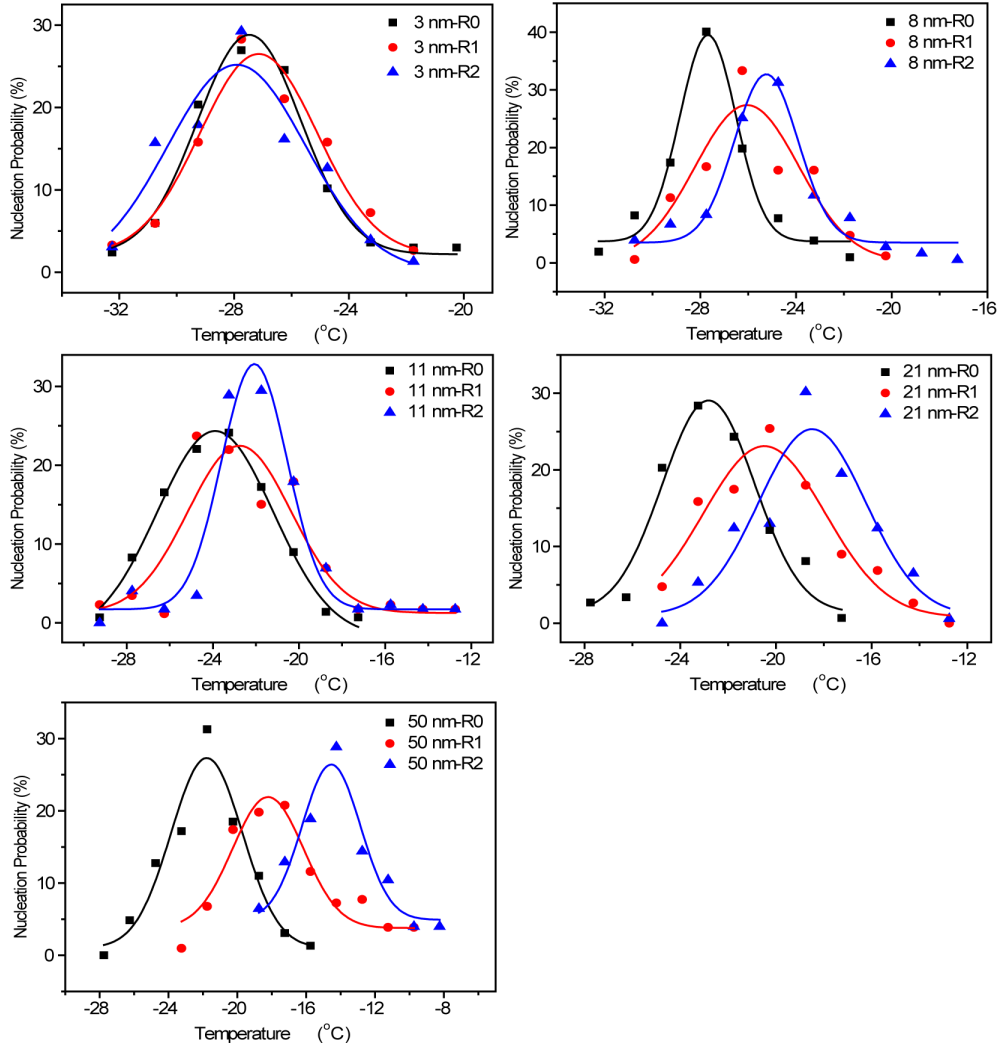
Supplementary Fig. 10 | Ice nucleation probability distribution (Gaussian fitting) of water droplets containing size-controlled GOs (0.52 µmol l⁻¹) of decreasing oxidation degrees. R0, R1 and R2 represent GO samples without alkali treatment and with alkali treatment at pH=10 and 12, respectively. The volume of an individual droplet is 0.2 µl. Cooling rate is 5 °C min⁻¹. For each distribution, the total number of the ice nucleation temperature measurement is about 150.
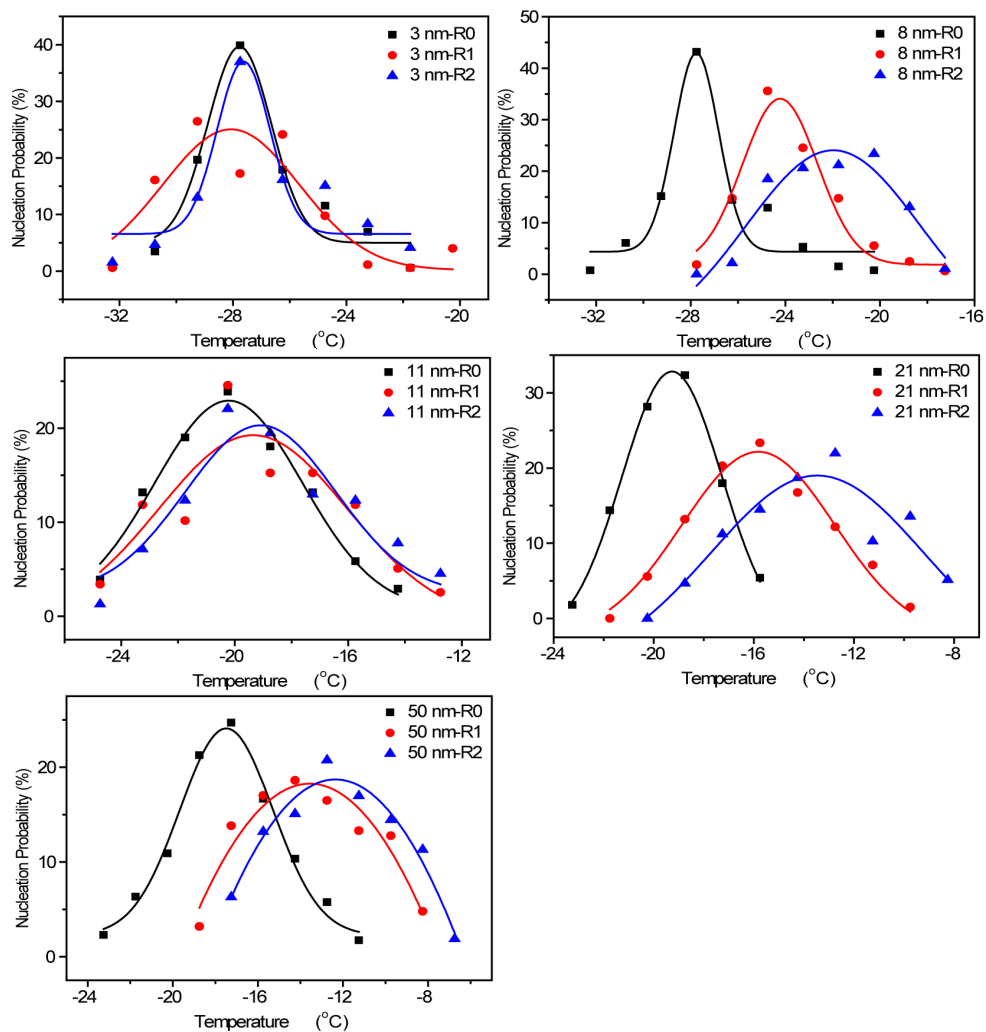
Supplementary Fig. 11 | Ice nucleation probability distribution (Gaussian fitting) of water droplets containing size-controlled GOs (5.2 µmol l⁻¹) of decreasing oxidation degrees. R0, R1 and R2 represent GO samples without alkali treatment and with alkali treatment at pH=10 and 12, respectively. The volume of an individual droplet is 0.2 µl. Cooling rate is 5 °C min⁻¹. For each distribution, the total number of the ice nucleation temperature measurement is about 150.
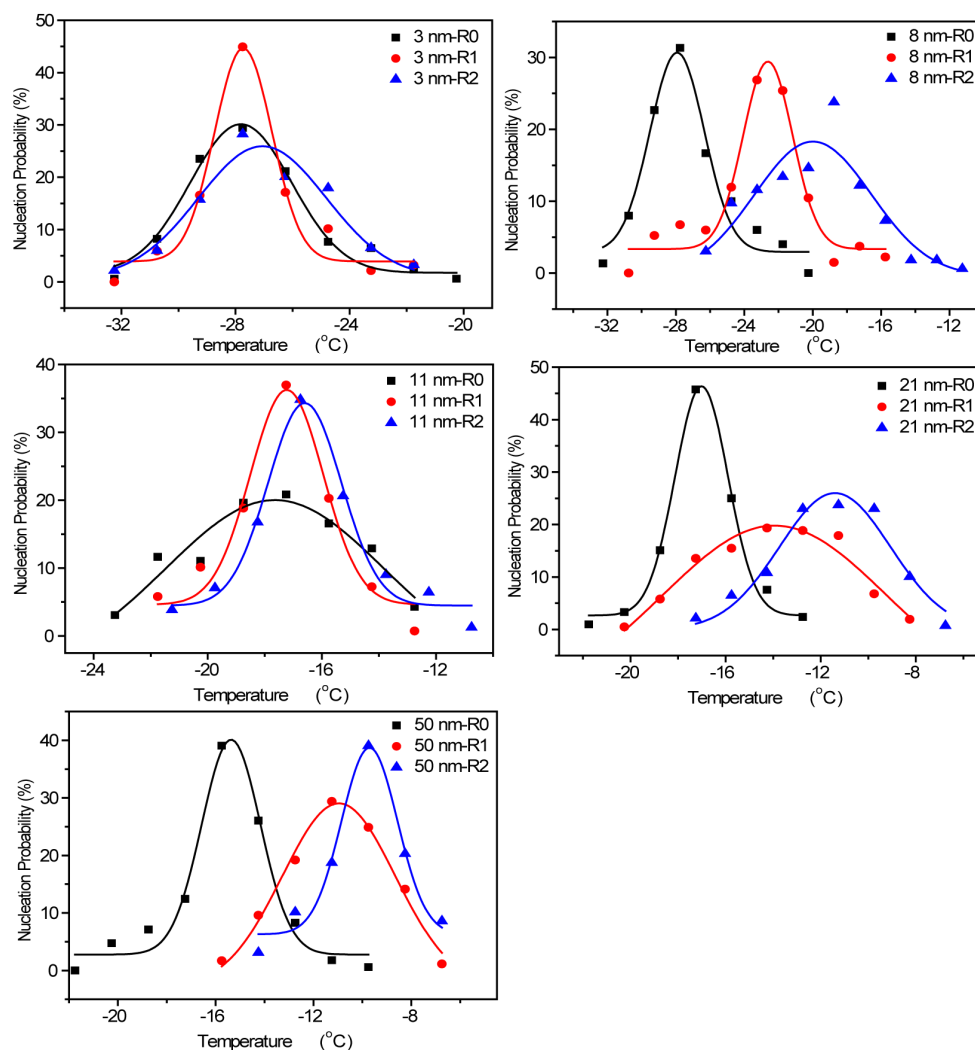
Supplementary Fig. 12 | Ice nucleation probability distribution (Gaussian fitting) of water droplets containing size-controlled GOs (13 μmol l⁻¹) of decreasing oxidation degrees. R0, R1 and R2 represent GO samples without alkali treatment and with alkali treatment at pH=10 and 12, respectively. The volume of an individual droplet is 0.2 μl. Cooling rate is 5 °C min⁻¹. For each distribution, the total number of the ice nucleation temperature measurement is about 150.

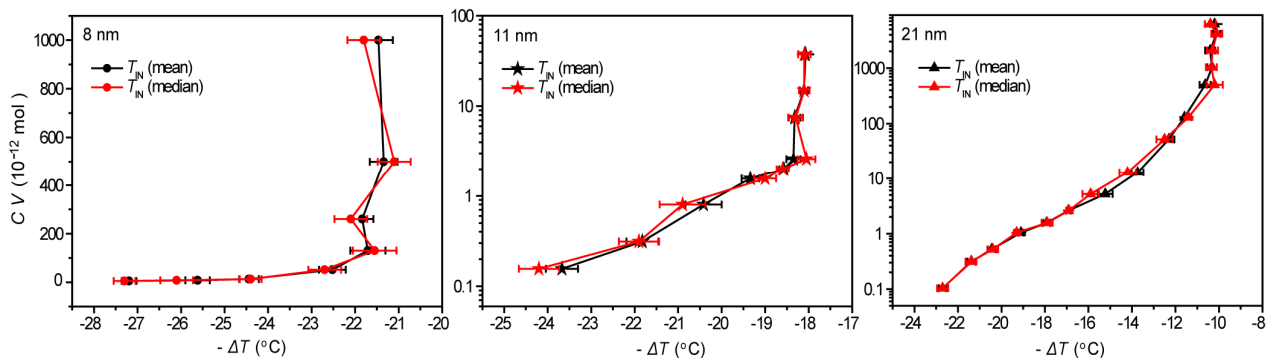**PS4: Tuning the T_{IN} of water droplets containing GOs by varying the number of GOs in water droplets.**

Supplementary Table 1. T_{IN} of water droplets containing different numbers (n) of GOs

| Size (nm)	C (µmol l^{-1})	V (µl)	$n = CV$ (10^{-12}mol)	T_{IN} (°C) (mean ± s.e.m.)
8 nm	5.2	1.0	5.20	−27.2 ± 0.2
	13	0.6	7.80	−25.6 ± 0.3
	13	1.0	13.0	−24.4 ± 0.2
	13	4.0	52.0	−22.5 ± 0.3
	13	10	130	−21.7 ± 0.4
	13	20	260	−21.8 ± 0.3
	50	10	500	−21.3 ± 0.3
	50	20	1000	−21.5 ± 0.3
11 nm	0.52	0.3	0.156	−23.7 ± 0.4
	0.52	0.6	0.312	−21.8 ± 0.4
	4	0.2	0.8	−20.4 ± 0.4
	5.2	0.3	1.56	−19.3 ± 0.2
	10	0.2	2.0	−18.6 ± 0.1
	13	0.2	2.6	−18.3 ± 0.2
	37.5	0.2	7.5	−18.3 ± 0.1
	75	0.2	15.0	−18.1 ± 0.1
	75	0.5	37.5	−18.1 ± 0.1
21 nm	0.52	0.2	0.104	−22.7 ± 0.2
	0.52	0.6	0.312	−21.4 ± 0.2
	5.2	0.1	0.520	−20.5 ± 0.2
	5.2	0.2	1.04	−19.1 ± 0.1
	5.2	0.3	1.56	−17.9 ± 0.2
	13	0.2	2.60	−16.9 ± 0.1
	5.2	1.0	5.20	−15.2 ± 0.3
	13	1.0	13.0	−13.7 ± 0.3
	13	4.0	52.0	−12.3 ± 0.3
	13	10	130	−11.6 ± 0.1
	50	10	500	−10.6 ± 0.3
	104	10	1040	−10.3 ± 0.2
	104	20	2080	−10.4 ± 0.2
	208	20	4160	−10.1 ± 0.2
	208	30	6240	−10.2 ± 0.2

The number of GOs (n) in water droplets was tuned by varying the concentration (C) of GO aqueous dispersion and/or droplet's volume (V). The molar concentration of GO is estimated from its mass concentration and molar mass (Methods). The volumes of small droplets of GO aqueous dispersions were determined using transferpettes. For each mean of T_{IN}, the total number of the measurements is about 50.

Supplementary Fig. 13 | The comparison between the mean ice nucleation temperature and the median ice nucleation temperature. Ice nucleation supercooling temperature of water droplets containing varying numbers ($n = CV$) of GOs with the same average lateral size L = 8 nm, 11 nm and 21 nm respectively. Here the cooling rate is always 5 °C min^{-1}. The error bars for the means and medians are s.e.m. and standard error of the median (estimated as 1.2533×s.e.m.), respectively. For each mean or median, the total number of the measurements is about 50. The difference between the mean and median ice nucleation temperatures is found to be small (less than 1 °C) in all our measurements.

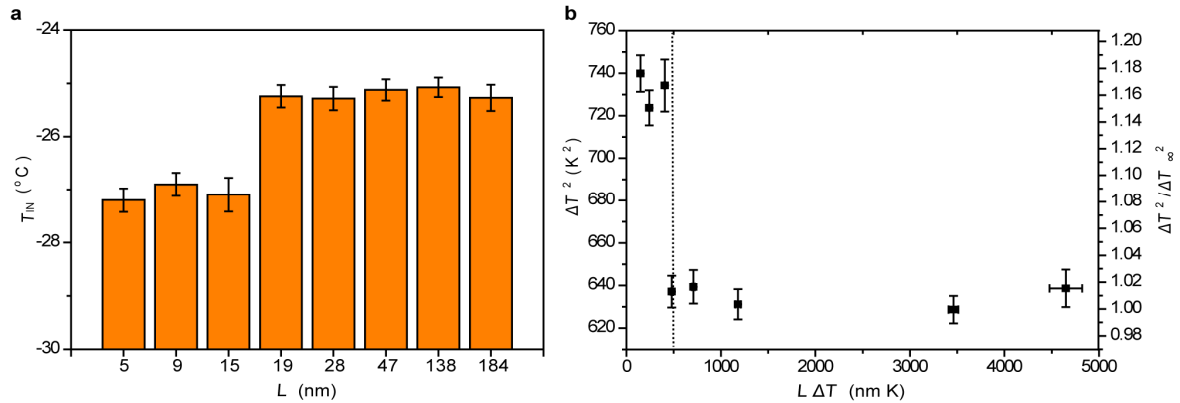**PS5: Size effect of Au nanoparticles on ice nucleation.**

Au nanoparticles of different sizes were purchased from Zhongke Au Research Technology Co. Ltd. (Beijing, China).
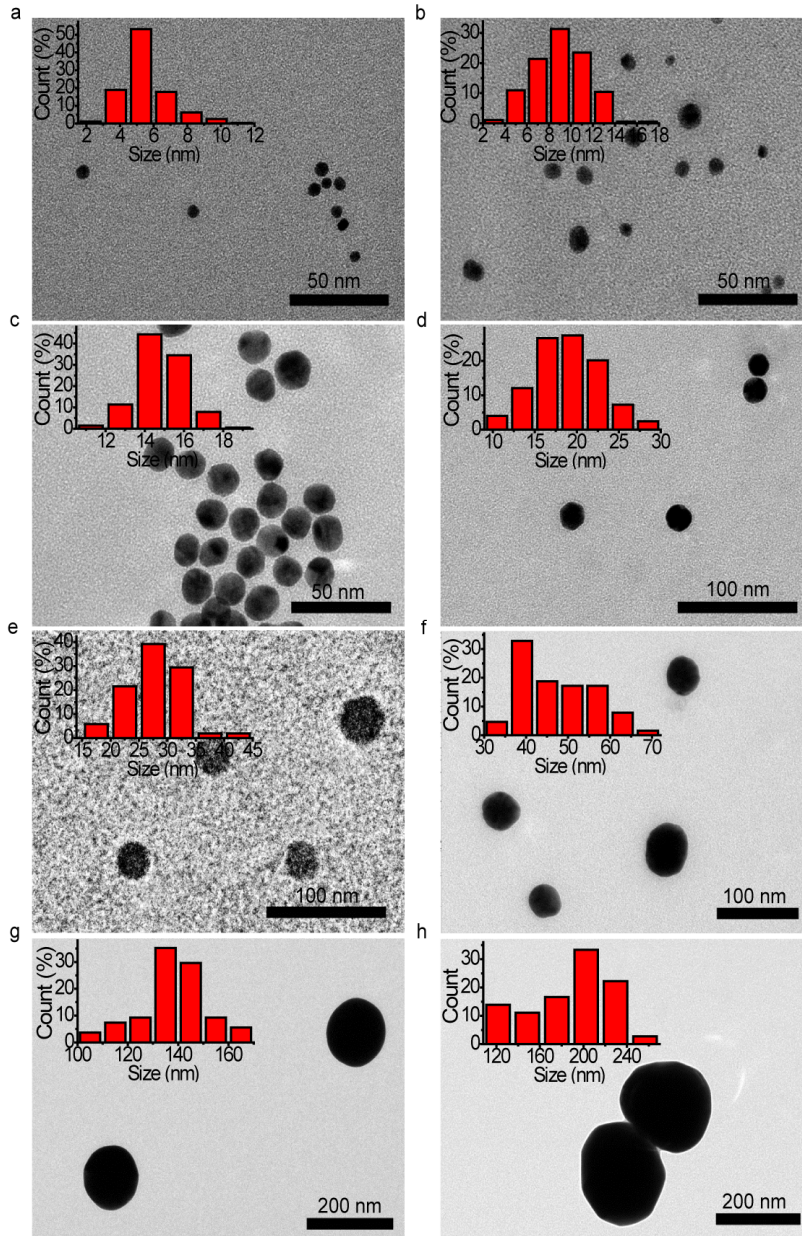
Supplementary Fig. 14 | Size characterization of Au nanoparticles. TEM images of Au nanoparticles with different sizes. The insets show the size distributions of corresponding Au nanoparticle samples measured by TEM. From **a** to **h**, the average sizes of Au nanoparticles are 5 ± 1, 9 ± 2, 15 ± 1, 19 ± 4, 28 ± 6, 47 ± 8, 138 ± 13 and 184 ± 41 nm, respectively. The error bars are s.d. with the total number of measurement of >100 for a, b, c, d, e and about 50 for f, g, h.
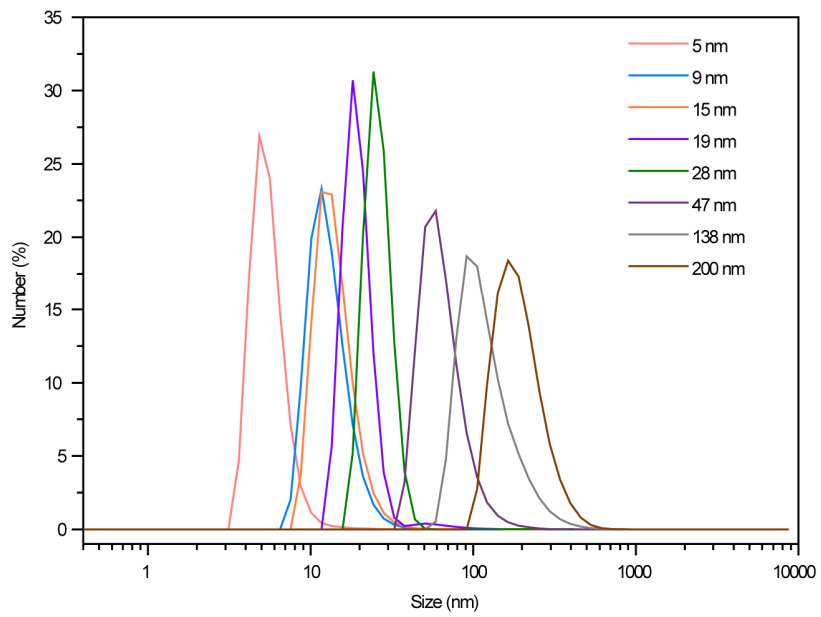
Supplementary Fig. 15 | Typical Hydrodynamic diameter distributions of Au nanoparticles. The measurements were performed by a Malvern Zetasizer (Nano ZS90, Malvern instruments Ltd., UK).

Supplementary Fig. 16 | Effects of the Au nanoparticle size on ice nucleation. a, The T_{IN} of water droplets (0.2 µl) containing Au nanoparticles with a series of average sizes: 5 nm, 9 nm, 15 nm, 19 nm, 28 nm, 47 nm, 138 nm and 184 nm. All the sample concentrations are 0.98 nmol L^{-1}. Cooling rate: 5 °C min^{-1}. Data are means ± s.e.m. For each mean of T_{IN}, the total number of the measurements is about 150. **b**, The relationship between ΔT^2 or $\Delta T^2/\Delta T_\infty^2$ ($\Delta T = T_m - T_{IN}$) and Au nanoparticle average size multiplied by supercooling temperature ($L\,\Delta T$). Here $\Delta T_\infty \approx 25$K is the nucleation supercooling on large nanoparticle under the same experimental conditions. The data are means and the error bars of ΔT^2 and $L\,\Delta T$ are calculated from the corresponding s.e.m. of T_{IN} and L based on the error propagation formulas. The results show that the T_{IN} increases abruptly when the size of Au nanoparticles increase to 19 nm. The corresponding $L\,\Delta T$ value is about 450 nm K in the case of Au nanoparticles.
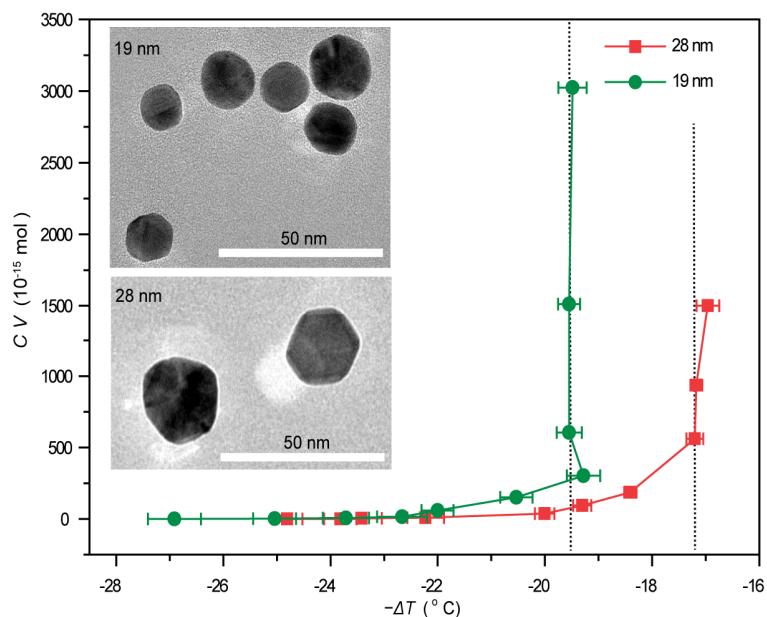
Supplementary Fig. 17 | The ice nucleation (supercooling) temperature $-\Delta T = T_{\mathrm{IN}} - T_{\mathrm{m}}$ **versus the number of Au nanoparticles in the water droplet.** The number of Au nanoparticles with the average size of 19 and 28 nm in water droplet was tuned by varying the concentration of Au aqueous dispersion (C) and/or the volume of the droplet (V). Here the cooling rate is always 5 °C min^{-1}. Data are means ± s.e.m. For each mean of T_{IN}, the total number of the measurements is about 50. The insets show the TEM images of these two types of Au nanoparticles.

Supplementary Fig. 17 shows that the abrupt change in the ice nucleation activities of gold nanoparticles occurs around $L\,\Delta T_L \approx 370$ nm K (for L=19 nm), and about 480 nm K (for L=28 nm), which are larger than that in the case of GO nanosheets, 200 nm K. It can be reconciled considering that gold nanoparticles are spherical-like and has some crystal planes with the lateral size smaller than the diameter of the sphere, as revealed by the TEM image. Therefore if the ice nucleation happens on the crystal planes, the lateral size of the crystal planes rather than the measured average diameter of gold nanoparticles should be correlated to ΔT_L, leading to the larger observed $L\,\Delta T_L$ value as we used the diameter of nanoparticles as L.

PS6: Theoretical analysis of ice nucleation activity of nanoparticles.
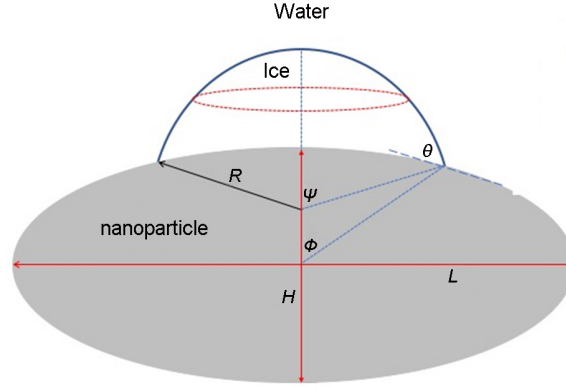
Supplementary Fig. 18 | The spherical-cap-like ice nucleus locates on a large oblate spheroid nanoparticle. The microscopic contact angle θ is the angle between the ice-water interface and the ice-nanoparticle interface. Ψ is the apparent contact angle of the ice nucleus.

Here we suppose that the nanoparticle is an oblate spheroid with the major diameter (lateral size) L, and the minor diameter (thickness) H. We define $l = \frac{L}{2R_c}$, and $\epsilon = \frac{H}{L}$. For the critical ice nucleus, the volume

$$V = \frac{4\pi}{3}[R_c^3 \, f(\Psi) - L^2 H \, f(\phi)].$$

The areas of ice-water interface and ice-substrate interface are,

$$S_{iw} = 2\pi R_c^2 (1 - \cos\Psi)$$

and

$$S_{is} = 2\pi L^2 \, \alpha(\phi; \epsilon).$$

Here $\alpha(\phi, \epsilon) = \int_{\cos\phi}^{1} \sqrt{x^2(1 - \epsilon^2) + \epsilon^2} dx$ is an ellipsoid integral. Ψ and ϕ are defined in Supplementary Fig. 18. The function $f(\psi) \equiv \frac{1}{2}(1 - \cos\psi) - \frac{1}{4}\sin^2\psi \cos\psi$ is the volume fraction of the plane-truncated spherical cap with any contact angle ψ. It is easy to know $\epsilon \tan\phi = \tan(\Psi - \theta)$, $l \sin\phi = \sin\Psi$, and $0 < \phi < \pi, 0 < \Psi < \pi$. Therefore, we have,

$$g(l, \epsilon; \theta) = \frac{3}{2}(1 - \cos\Psi) - \frac{3}{2}\alpha(\phi; \epsilon) l^2 \cos\theta - 2f(\Psi) + 2f(\phi) l^3 \epsilon.$$

and the free energy barrier $\Delta G^*(\Delta T; L, H, \theta) = \Delta G_{hom}^*(\Delta T) \, g(l, \epsilon; \theta)$, where $\Delta G_{hom}^* = \frac{16\pi\gamma^3}{3|\Delta\mu|^2}$ is the free energy barrier of the homogeneous ice nucleation.

For large nanoparticle ($L \gg 2R_c, or\ l \gg 1$), $\Psi \to \theta$, we have $g(l \gg 1, \epsilon; \theta) \to f(\theta)$. Thus the free energy barrier equals to that of the normal heterogeneous nucleation on a sufficient large flat-plane substrate $\Delta G^*_{het} = \Delta G^*_{hom} f(\theta)$. While l approaches to zero, $\Psi \to \pi$, thus $g(l \to 0, \epsilon; \theta) \to 1$, *i.e.,* the free energy barrier equals to that of the homogeneous nucleation.

As shown in Supplementary Fig. 19 and 20 we illustrate the dependence of $\hat{g}(l, \epsilon; \theta) \equiv \frac{g(l,\epsilon;\theta)}{f(\theta)}$ on the size of nanoparticles for some typical parameters $\theta = 20^o, 25, 30^o$, and $h \equiv \frac{H}{2R_c} = 0.2,\ 0.3$, and on a spherical particle ($h = l, or\ \epsilon = 1$). For a large range of the parameters, the free energy barrier on the finite-sized GO shows an obvious transition around $l_c \sim 1$. When $l > l_c$, the free energy barrier is almost a constant, and equals to that of the heterogeneous nucleation on infinite flat substrate, thus $\hat{g}(l, \epsilon; \theta) \sim 1$; but it abruptly increases as l approaches l_c.
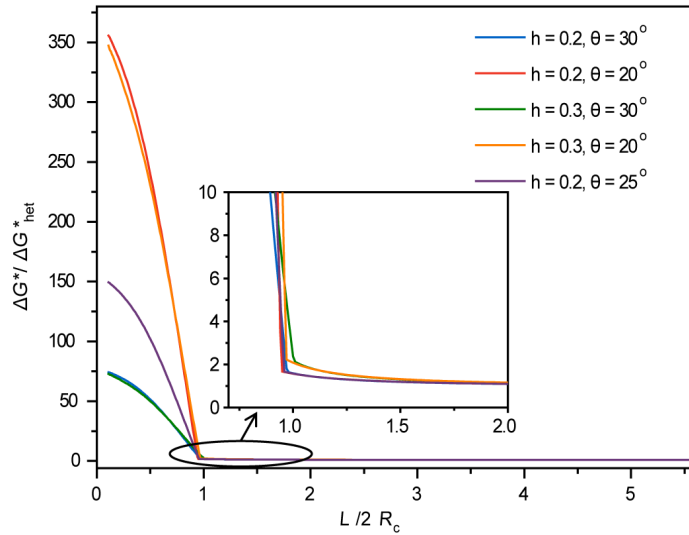
Supplementary Fig. 19 | The variation of free energy barrier of ice nucleation with the change of the nanoparticle size. The relationship between $\Delta G^*/\Delta G^*_{het}$ and $L/2R_c$ when nanoparticle is modeled as an oblate spheroid with major diameter (lateral size), L, and minor diameter (thickness), H, respectively. $h \equiv \frac{H}{2R_c}$. The figure shows the typical curves when $\theta = 20^o, 25, 30^o$, and $h = 0.2,\ 0.3$. The inset is the detail of the curves around $L = 2R_c$.
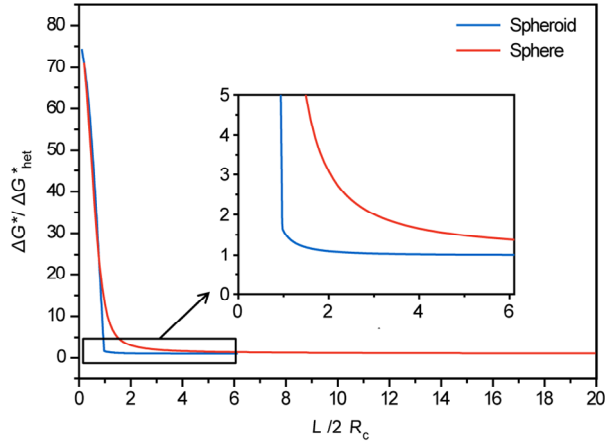
Supplementary Fig. 20 | The dependence of free energy barrier of ice nucleation on the size of oblate spheroid or spheroid particles. The relationship between $\Delta G^*/\Delta G_{het}^*$ and $L/2R_c$ for an oblate spheroid (take $h \equiv \frac{H}{2R_c} = 0.2$ as an example) or spheroid particles. L is the major diameter of oblate spheroid particles or diameter of spheroid particles. H is the minor diameter of the oblate spheroid particle. Here, we take $\theta = 30^o$ as an example. The inset shows the detail of the curves.

If the nanoparticle has another shapes, we can follow the same idea listed here to calculate the free energy barrier. For example, for a thin disc with smooth semi-circle edge, which was applied in the main text, it is direct to calculate the free energy of ice nucleus and the shape of ice nucleus by following the same spirit applied in sphere or oblate spheroid nanoparticles.

PS7: References.

1. Yang, D. et al, Chemical analysis of graphene oxide films after heat and chemical treatments by X-ray photoelectron and Micro-Raman spectroscopy. *Carbon* **47**, 145–152, doi: 10.1016/j.carbon.2008.09.045 (2009).

2. Chen, J. et al. Size fractionation of graphene oxide sheets via filtration through track-etched membranes. *Advanced Materials* 27, 3654–3660, doi:10.1002/adma.201501271 (2015).

3. Geng, H. *et al.* Size fractionation of graphene oxide nanosheets via controlled directional freezing. *Journal of the American Chemical Society* **139**, 12517–12523, doi:10.1021/jacs.7b05490 (2017).

4. Cai, W. et al, Synthesis and solid-State NMR structural characterization of ^{13}C-labeled graphite oxide. *Science* **321**, 1815–1817, doi: 10.1126/science.1162369 (2008).

5. Algarra, M. et al. Enhanced electrochemical response of carbon quantum dot modified electrodes. *Talanta* **178**, 679–685, doi: http://dx.doi.org/10.1016/j.talanta.2017.09.082 (2018).

6. Kudin, K. N. et al, Raman spectra of graphite oxide and functionalized graphene sheets. *Nano Letters* **8**, 36–41, doi: 10.1021/nl071822y (2008).

7. Lucchese, M. M. et al. Quantifying ion-induced defects and Raman relaxation length in graphene. *Carbon* **48**, 1592–1597, doi:10.1016/j.carbon.2009.12.057 (2010).

8. Cancado, L. G. et al. Quantifying defects in graphene via raman spectroscopy at different excitation energies. *Nano Letters* **11**, 3190–3196, doi:10.1021/nl201432g (2011).